

A Low-Cost Articulated Arm Navigation System for External Ventricular Drain Placement

Alexander D. Smith^{1,2}, IEEE Student Member, Anant Naik³, Suguna Pappu^{2,4},
Paul M. Arnold^{2,5}, and Kris Hauser¹, IEEE Senior Member

Abstract—Objective: This paper proposes a low-cost real-time navigation system to assist a surgeon in placing external ventricular drains. **Methods:** In our approach, the base of an articulated arm coordinate measuring machine is bolted to the patient’s skull, and a graphical user interface quickly guides the operator through the image registration and 3D navigation to place an external ventricular drain at a desired target specified relative to preoperative imaging. The method can be employed in workflows with and without fiducials embedded in the preoperative imaging. **Results:** The proposed system is evaluated using precise registration instruments, human phantom models, and ex vivo ovine models, demonstrating less than 2 mm of error with fiducials and less than 4 mm of error without fiducials. **Conclusion:** The registration procedure takes less than one minute and can be performed intuitively by a single operator without an assistant. **Significance:** Our proposed system enables real-time image-guided navigation to be used in bedside external ventricular drain placement, with potential to expand access to this procedure.

Index Terms—Neurosurgery, External ventricular drain, Neurosurgical navigation, Registration, Articulated Arm Coordinate Measuring Machine

I. INTRODUCTION

External ventricular drains (EVD) are placed in patients with increased intracranial pressure to divert cerebrospinal fluid from the intracranial space, alleviating pressure and providing neurological stabilization [1]. They are used most often for patients with moderate and severe traumatic brain injury (TBI), hydrocephalus, stroke, and tumors. After one of these neurological events, proper and timely intervention with an EVD is critical to minimize patient morbidity or mortality [2]. Complications resulting from misplaced EVDs can be severe, including fatalities or permanent disability [3].

Emergency EVDs are placed using a freehand approach at the bedside in over 42,000 cases annually in the United States [4]. In recent decades, several devices, notably the Ghajar guide [5] among other passive guides and frames have been proposed to increase the viability of a non-neurosurgeon provider performing EVD placement [6].

¹Department of Computer Science at the University of Illinois at Urbana-Champaign, Urbana, Illinois, USA. ads10@illinois.edu, kkhauser@illinois.edu

²Carle Illinois College of Medicine at the University of Illinois at Urbana-Champaign, Urbana, Illinois, USA

³Department of Neurosurgery at University of Minnesota Twin-Cities, Minneapolis, Minnesota, USA

⁴Department of Neurosurgery at Carle Foundation Hospital, Urbana, Illinois, USA

⁵Department of Neurosurgery at Loyola University Medical Center, Maywood, Illinois, USA

Studies show that navigation in EVD placement with electromagnetic or optical trackers is superior in accuracy compared to the freehand approach [7]. The rate of accurate freehand placement of an EVD is reported as low as 40% [8], whereas navigated placement using real-time image-guided navigation systems, such as the StealthStation AxiEM or StealthStation S7, is shown to improve accuracy to 95%. Moreover, image-guided navigation reduces the mean number of passes required to successfully place an EVD from 1.63 to 1.16 [7]. Navigation is particularly helpful in challenging anatomy, especially in midline brain shift and “slit ventricles”, in which brain anatomy is distorted by pathology. Bedside ultrasound approaches for EVD placement have been explored previously, but require large or modified burr holes or unfamiliar workflows [9, 10]. More cost-effective EVD placement approaches aimed at low- and middle-income countries (LMIC) have been explored, including simple drain guides [5, 11] and more advanced drain guides [12, 13, 14, 15, 16, 17]. While these newer systems show promise, none have been shown to address the education and resource gaps in providing emergency EVD intervention in these regions [18]. There remains a long-standing need to develop a simple, intuitive, and safe approach to assist providers with emergency intracranial pressure relief for acute hydrocephalus, particularly in LMIC [19].

To design a system to meet this need, we propose the following design criteria:

- **Cost:** Hardware, including the cranial access kit, must cost less than \$2,500 to produce.
- **Accuracy:** Tracking accuracy of an effector-mounted EVD tip must be within 5 mm of a target location following registration.
- **Time:** The use of navigation should add no more than 5 minutes to the freehand EVD placement approach.
- **Usability:** The system must be ergonomic and easily operable by a single user such that EVDs can be placed at the bedside.
- **Interactivity:** The interface must provide real-time instruction to guide the operator through the procedure.

This paper presents a real-time surgical navigation system based on an articulated arm coordinate measuring machine (AACMM) that shows promise in meeting each of the above objectives (Figure 1). The 4-joint Arm is mounted to the skull and registered to preoperative imaging in a single operator procedure. Our App visually guides the operator through the

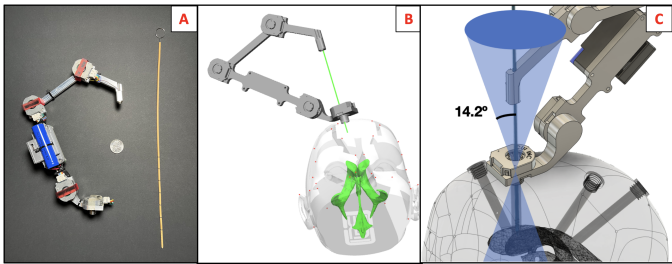


Fig. 1. A) The Arm (left) depicted with External Ventricular Drain (right) and USA quarter for scale. B) 3D visualization App with a phantom, highlighting targeted anatomy for the surgical operator. C) Reachable workspace with a maximum tilt of 14.2° through the bolt.

registration procedure and provides real-time 3D EVD position tracking. Our primary hardware innovations include a self-tapping skull bolt with a through-hole, which provides rigid fixation of the device to the skull within the existing bedside EVD placement procedure, and a registration probe that provides an accurate method to map surface features through skin or fiducial contact. Our software provides real-time 3D visualization and hands-free guidance through registration and drain navigation with respect to a registered 3D medical image. Our system is compatible with two registration pipelines: a fiducial-based and a surface-based (fiducial-free) method. The fiducial-based method requires a more invasive and lengthy preoperative setup, but provides higher overall accuracy.

The accuracy of our system is validated with multiple methods, including theoretical accuracy using calibrated reference targets, and end-to-end accuracy through registration using a phantom model and an ex vivo ovine model. Experiments on the phantom demonstrate sufficient accuracy of our system for drain placement using surface-based registration (< 4 mm error) and even higher accuracy with fiducial-based registration (< 2 mm error). An ex vivo sheep head study shows that accuracy of our system is maintained in real tissue with 2.765 ± 1.121 mm error implanting needles to an average depth of 42.23 ± 3.03 mm into the brain. Moreover, a user interface pilot study on medical trainees and professionals shows that the registration workflow can be completed consistently in under 1 minute, with an overall simulated EVD placement completed consistently in under 2 minutes.

II. RELATED WORK

Surgical navigation systems provide surgeons with real-time visualization of surgical tools relative to patient anatomy, and include stereotactic frames, ultrasound probes, optical systems, and electromagnetic trackers [20]. Often, screens show tracked surgical tooling overlaid on preoperative imaging [21], and augmented reality can display these elements within the surgeon's field of view [22] [23]. AACMMs were also explored briefly in the 1990's for use in navigation [24, 25]. These systems were designed to be mounted to a head clamp and had six joints to allow for six degrees of freedom (DOF) tool motions within a confined workspace. Prior AACMM systems were cumbersome, required many components, and were historically overshadowed by optical navigation systems [26]. Our paper addresses these limitations by using a single burr

hole-mounted bolt to rigidly affix a small AACMM to the skull. Our system software and hardware enables a single operator to perform the entire installation, registration, and navigation workflow. Our system can fit within a specialized bedside cranial access kit and requires only minor adjustment to existing surgical workflows.

Existing real-time surgical navigation products are expensive, require significant infrastructure such as electromagnetic trackers or optical trackers, and are challenging to introduce into emergency conditions [27, 28]. Hence, many neurosurgeons from rural settings will opt for invasive but consistent approaches, such as decompressive craniectomy, for intracranial pressure management [29]. Prior approaches for low-cost surgical navigation in underserved settings include optical approaches such as the NousNav system designed for operating room use [30], and custom drain guides [13]. Drain guides are similar in scope to the Ghajar guide, an instrument developed in the 1980s with limited adoption due to concerns about accuracy [31].

Neuronavigation requires 1) preoperative medical images to be obtained with CT or MRI, 2) a means of rigidly tracking anatomy, and 3) a method to perform image registration. Mechanisms for rigidly tracking anatomy include skin or bone mounted reference frames [33]. Registration methods use either fiducial markers or detected surface features to determine alignment of the reference frame with a preoperative image [34]. Fiducial methods determine the alignment of the device with patient imaging by detecting fiducial markers placed on the skin or screwed into the skull before preoperative imaging is captured [35, 36]. Surface feature detection does not require a fiducial placement step, and instead involves the collection of points of the patient's face or other anatomy to align with an image segmentation of the CT scan or MRI [37]. Both approaches are supported by our proposed work, and our experiments are consistent with prior results demonstrating that skull-mounted fiducials lead to higher accuracy [38]. However, our results suggest that surface-based registration provides adequate accuracy for EVD placement.

The concept of mounting a miniature AACMM to the skull to assist in EVD placement was introduced in work by the authors and colleagues [32, 39, 40]. A five-joint, four degrees-of-freedom (DOF) AACMM was originally proposed with an Arduino microcontroller and wireless communication to a laptop [39]. Following the initial work, Borovik expanded on the design of the original system by removing the redundant fifth joint and implemented a user interface that displayed the position of a drain in medical image slices [40]. However, their mechanism did not meet the accuracy and repeatability metrics necessary to perform EVD placement in one out of three experiments, lacked in stability, and had no method of mounting their device to a human skull. The AACMM proposed in [32] was mostly conceptual, and was not evaluated in the context of registration workflows.

In relation to prior work, our contributions in this paper include: a prototype with improved tracking precision, a bolt for rigid fixation to the skull, a touch-activated registration

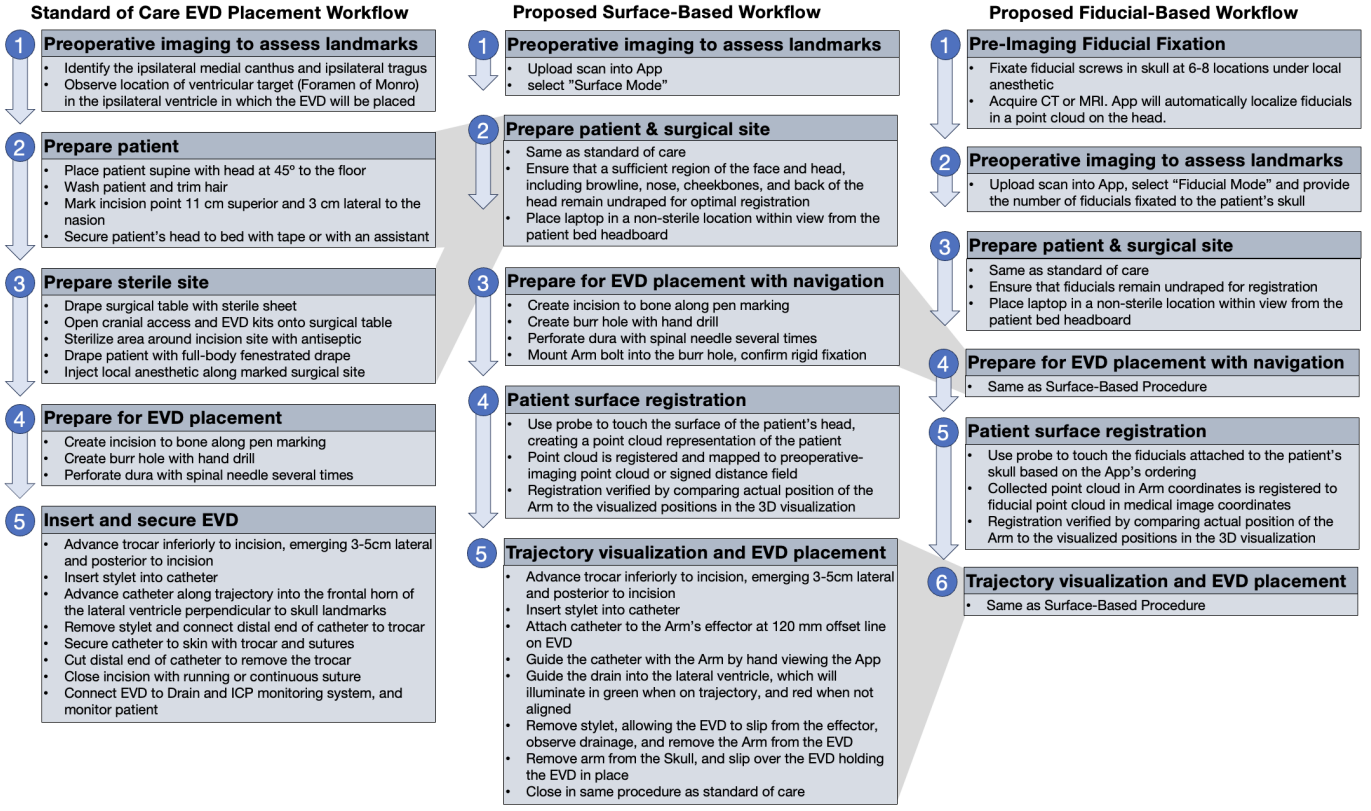


Fig. 2. The three procedural workflows described in this work. The left column describes a typical standard of care approach for bedside EVD placement. The middle column describes our proposed surface-based workflow, and the right column describes our proposed fiducial-based workflow. This figure is an updated version of our previous proposed workflow shown in Figure 7 of [32].

probe for single-operator feature acquisition, workflows for bedside navigation of EVD placement, software with 3D visualization for procedural guidance through the workflows, and an evaluation of end-to-end system accuracy through the entire registration and EVD placement workflow.

III. APPROACH AND METHODS

Our navigation system consists of the *Arm*, an AACMM built from the components in Table I, and the *App* that walks the surgeon through the setting up the procedure, using the AACMM, and performing the surgery. The visualization software can be run on any standard PC or Android tablet and displays real-time 3D navigation feedback on a monitor within view of the surgical field.

A. Surgical workflows

In freehand EVD placement, a neurosurgeon starts by identifying the trajectory needed to insert a drain from Kocher's point to the frontal horn of the lateral ventricle on preoperative imaging [1]. Kocher's point is marked 10-11 cm posterior and 3 cm lateral to the nasion [41], and the patient's head is then held by supporting personnel or secured to the bed. The surgical procedure then commences, following the steps outlined in Figure 2, left.

We propose two similar surgical navigation workflows for navigated bedside EVD placement with our system. The first is a surface-based workflow, in which the surface of the patient's

skin is traced by a probe located on the effector of an AACMM and geometrically mapped to the patient's pre-surgical imaging in 3D (Figure 2, middle). The second is a fiducial-based workflow, in which several fiducials are implanted into the skull before acquiring the preoperative medical image, and these fiducials are collected in a specified order by the probe and used to perform registration to preoperative imaging (Figure 2, right).

B. Arm Hardware Design and Assembly

The *Arm* is an AACMM with an approximately spherical workspace roughly 28 centimeters in diameter, which intersects about 50% of the volume of the average human skull when mounted, providing sufficient reach to perform surface-based registration by touching facial features. The device is constructed from inexpensive components including rotary encoders, a Raspberry Pi, lithium-ion batteries, 3D printed parts, and machined aluminum. The bill of materials for this prototype costs under \$2,500, which primarily consists of custom machining costs. When assembled, the *Arm* weighs 348 g. Five links and four rotary joints provide the catheter with four DOF, two translational and two rotational, which constrains motion to the same DOF available to a user performing freehand EVD placement (Figure 1C). Rotary encoders are used to capture joint angles using the Raspberry Pi's serial peripheral interface (SPI) bus. The program relays 14-bit encoder positions over a wireless TCP/IP socket at between 250 and 280 Hz,

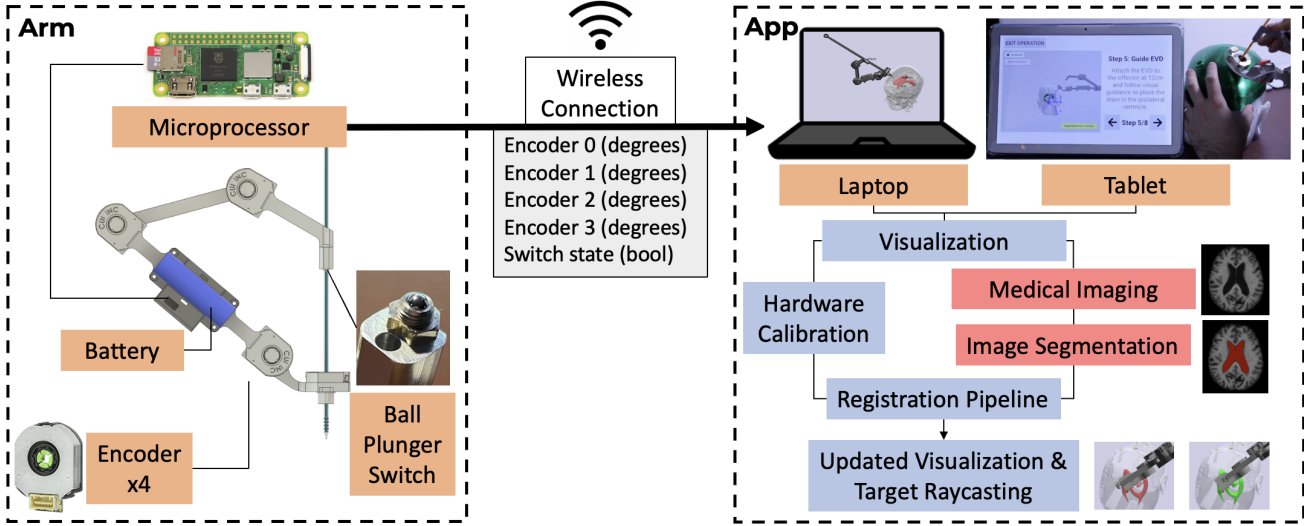


Fig. 3. Block diagram for our neurosurgical navigation system. The *Arm* encodes the position of each joint with four capacitive rotary encoders and relays this information across a wireless channel. A laptop or tablet running the visualization environment processes the encoded position of each link and calculates the effector location, allowing for navigation of the effector relative to the skull bolt.

enabling real-time position acquisition and visualization of the kinematic structure. We use forward kinematics to update the model position and navigation aids in real-time in the virtual environment based on encoder positions.

We designed the skull bolt with an inner bore of 9 mm, external M12x1.75 thread with a 2 mm chamfer at the bottom edge to tap and rigidly fix into bone. The inner bore allows 14.2° of drain angulation offset from the axis of the bolt. The effector mount is designed with a 3.4 mm bore to rigidly mount a Codman Bacteriseal EVD to the effector with friction when a stylet is inserted. The drain will slip from the effector mount when the stylet is removed due to a drop in friction between the outer surface of the EVD and the wall of the bore.

The registration probe consists of a ball-plunger switch located axially on the effector of the system. The switch is depressed on the face or fiducials to collect features during registration. The ball rolls smoothly along a surface, preventing it from snagging on the skin or hair, and it can interface with divots of a smaller diameter than the ball. Divots, such as the circular hole in a Waypoint Fiducial in the Starfix skull reference frame system [42], can be localized precisely by activating the switch when the ball is interfaced with the hole. The probe exhibits 0.3 mm of depth travel before its internal switch is activated. When the switch is activated, the *App* computes the Cartesian position of the center of the ball relative to the base of the *Arm*. These points are used in our registration processes to map the *Arm* base frame to the imaging frame.

All interfacing surfaces and lengths of the machined parts are designed with a tolerance of 0.05mm. Forward kinematics are calculated using the CAD model link lengths. The encoders are daisy-chained and connected to one Raspberry Pi SPI bus with the registration probe connected to a digital I/O pin. A second I/O pin is wired to a header from which the testing probe can be connected and disconnected during operation. All components used for the hardware are detailed in Table I.

TABLE I
MATERIALS USED

| Component | Part Used |
|--------------------|---|
| Laptop | Dell XPS 13 9343 with Intel i5-5200U |
| Tablet | Zonko D106 with Android 14.0 |
| Microcontroller | Raspberry PI Zero 2 W |
| Encoders (x4) | CUI AMT 222B-V |
| Registration Probe | Misumi BP5MWA ball switch |
| Voltage Booster | Adafruit PowerBoost 500c |
| Battery | 2200 mAh lithium ion |
| Links | Machined 6063 aluminum |
| Skull Bolt | Machined stainless steel |
| Case and Clips | 20g FDM 3D printed plastic |
| Miscellaneous | Zip ties, 30 AWG cable, M2.5 bolts & nuts |

C. App Design

The *App* provides a user interface for simulated visualization and navigation throughout the medical image segmentation with the *Arm*. Our implementation runs on a laptop (Dell XPS 13 running Ubuntu 22.04 with 8 GB of RAM and an Intel Core i5-5200U processor) or a tablet (Zonko D106 8-core running Android 14.0). Figure 3 illustrates the communication protocol between the *Arm* and the *App*.

1) *User Interface*: The *App* user interface instructs the user through non-sterile setup and a sterile procedure. The non-sterile setup includes 1) loading relevant patient anatomy into the *App*, and 2) powering up and connecting the *Arm*. Patient imaging is initially loaded into the *App*, requiring a 3D segmentation of the surface of the skin and the EVD placement target (i.e., lateral ventricle). Automated segmentation methods for these features exist for CT and MRI imaging modalities [43, 44]. To obtain a skin surface segmentation mesh of a CT scan, 3D Slicer [45] is used to add all voxels with an intensity greater than -160 Hounsfield units to a segmentation, the largest connected component is identified and isolated, and the flying edges algorithm is used to obtain a surface mesh

[46]. For phantom evaluation, we skip the imaging step and instead load the CAD models used to construct the phantoms.

The user interface then guides the user through the sterile procedure, in which the user performs 1) surgical preparation including creating the burr hole at Kocher’s point, 2) attaching the *Arm* to the burr hole, 3) feature acquisition and registration, 4) guidance and successful placement of the EVD, and 5) removal of the *Arm* and surgical closure [32]. If surface registration is selected, a heatmap of reachable surface regions for surface-based registration is provided in the *App* during the feature acquisition step. If fiducial registration is selected, the *App* will illuminate the current fiducials to be collected in order.

2) *Registration Methods*: We implemented three registration methods: fiducial registration [47], point cloud to point cloud iterative closest point (PC2PC ICP) [48, 49], and our own point cloud to surface iterative closest point method (PC2SDF ICP).

Before registration, two feature sets must be acquired: one from the patient’s medical image, and one from the system’s measurements. Both of these feature sets must correspond to overlapping regions of the patient for registration to be successful. The medical image feature set is acquired differently for our three registration formulations, and the operator utilizes the registration probe based on the selected registration formulation. The operator will control the *Arm*, guiding the registration probe to locations based on the features they intend to collect - surfaces or fiducials. The *App* calculates the forward kinematics of the *Arm* based on the encoder measurements, updating the position of the joints in the *App*’s visualization interface. The position of the point located at the center of the registration probe ball is computed relative to the position of the base of the *Arm* whenever the probe is depressed using the forward kinematic model. These points collected by the registration probe ball are added to a point cloud, which acts as the second feature set in the registration methods. These points are then matched to target points from the medical image feature set along the normal direction by the radius of the ball.

Because fiducials are collected in a specified order, the fiducial registration method involves the calculation of a least-squares fitting between two point sets of known correspondences. We implement the classical SVD approach devised by Arun, et al. [47] to solve the fiducial registration problem. The fiducial registration process follows the top row of Figure 4.

For PC2PC ICP, we first convert a mesh of the surface of the head into a point cloud using Poisson disk sampling, dispersing points relatively uniformly with a spacing of approximately 1-2 mm [50]. The surgeon will first collect three predefined points representing the tip of the nose, the nasion, and the midpoint of the left brow based on relative positions in the CT scan, then our fiducial registration approach is utilized to find a coarse initial guess of the registration. The coarse guess prevents ICP from becoming trapped in local minima. Then, the surgeon traces the surface of the patient’s head with the registration probe, which takes approximately

Algorithm 1 General Iterative Closest Points (ICP)

```

1: Initialize transformation  $T_0 = I$  (identity matrix)
2: Set a convergence threshold  $\epsilon$ 
3: Set a maximum number of iterations  $max\_iterations$ 
4: Set iteration count  $i = 0$ 
5: while not converged and  $i < max\_iterations$  do
6:    $P' \leftarrow T_i \cdot P$  {apply transformation to source points}
7:   Update correspondences with Algorithm 2 or 3
8:   Compute the optimal transformation  $(R, t)$  using the
    method described by Arun, et al. [47]
9:   Update the transformation  $T_{i+1} \leftarrow \begin{bmatrix} R & t \\ 0 & 1 \end{bmatrix} \cdot T_i$ 
10:  Check for convergence:
11:    if  $\|T_{i+1} - T_i\| < \epsilon$  then
12:      Converged  $\leftarrow$  True
13:    end if
14:     $i \leftarrow i + 1$ 
15:  end while
16: return  $T_i$ 

```

10 seconds. Next, our ICP determines corresponding closest points between the source P , representing the surface point cloud traced by the registration probe, and target Q , representing the sampled point cloud from the mesh, by calculating the point in Q closest to the point p_i in P . We update the transformation, applying the correspondence calculation to the transformed source point cloud P' . We then iterate until reaching a convergence threshold or when the number of iterations has elapsed. The PC2PC registration process follows the central row of Figure 4.

Algorithm 2 PC2PC Correspondence Function

Input: Transformed source $P' = \{p'_1, p'_2, \dots, p'_n\}$, Target point cloud $Q = \{q_1, q_2, \dots, q_m\}$

```

1: for each point  $p'_i \in P'$  do
2:   Find closest point  $q_j \in Q$ 
3:   Associate  $p'_i$  with  $q_j$ 
4: end for
5: return Associations

```

In PC2SDF ICP, we use the same point collection procedures as in PC2PC ICP, however, we implement a specialized ICP approach using the surface mesh in place of the ICP method for 3D shapes as described by Besl et. al [48]. The surface mesh of the patient anatomy is converted to a signed distance field, and the closest points on the surface of the mesh are queried relative to each of the points in the traced point cloud. We then apply least-squares fitting between the queried and traced point clouds. On each iteration, the closest points between the signed distance field and the traced point cloud are resampled, and the fitting is repeated until the registration error drops below a threshold or a number of iterations has elapsed. The PC2SDF registration process follows the bottom row of Figure 4.

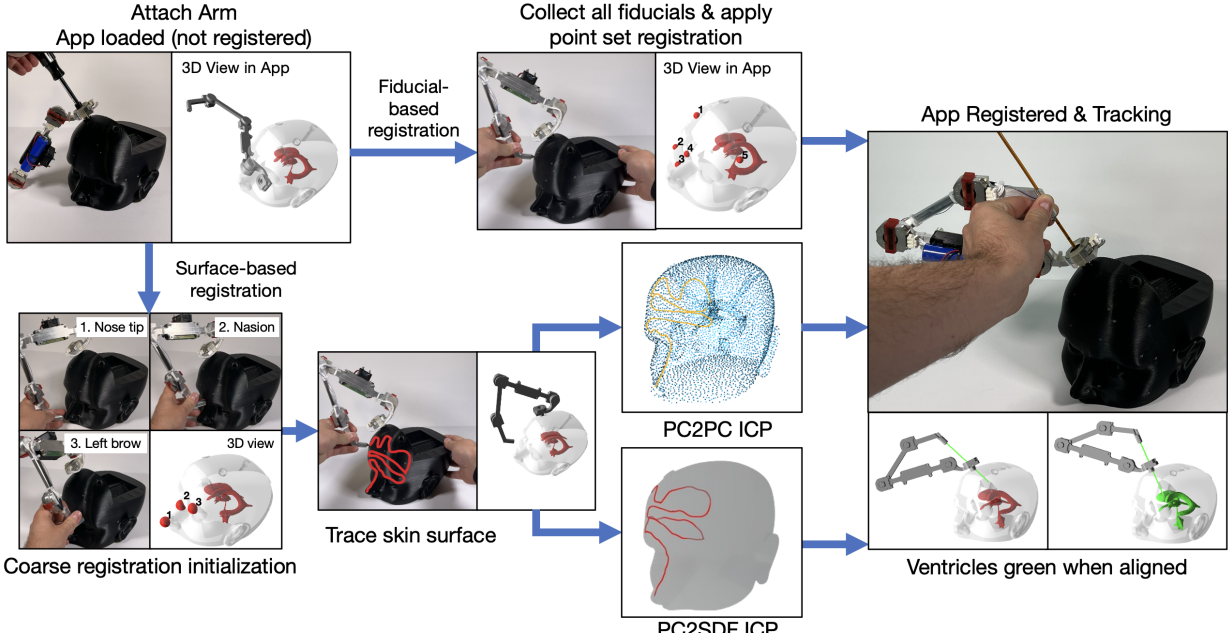


Fig. 4. Registration procedures. Both procedures start by attaching the *Arm* to the patient's skull. In fiducial-based registration, the fiducials are collected in a specified order, then the *App* is updated to visualize the *Arm* registered and overlaid on the medical image. In surface-based registration, a coarse fiducial-based registration is performed to create an initial alignment, then the surface is traced to act as a surface to fit. Then a choice of point-cloud or signed distance field is used as a representation of the medical image surface target, and an iterative registration is performed. After registration, ray tracing is used to illuminate the target anatomy (ventricles) in green when the effector's z-axis is aligned with the target.

Algorithm 3 PC2SDF Correspondence Function

Input: Transformed source $P = \{p_1, p_2, \dots, p_n\}$, Target signed distance function f

- 1: **for** each point $p'_i \in P'$ **do**
- 2: Find the point q_j on the surface defined by f closest to p'_i by minimizing the distance $f(q_j)$
- 3: Associate p'_i with q_j
- 4: **end for**
- 5: **return** Associations

3) *Surface accessibility heatmap generation:* Due to the *Arm*'s 4DOF constraint, the registration probe cannot reach all points on the head and/or align perpendicularly to the skin surface. Accessible regions may differ somewhat between patients that range in morphology and pathology. So, to indicate this to the operator, a visual heatmap is used to visually indicate where the registration probe interfaces appropriately or poorly at a selected point on the surface of the skull. The operator may choose to visualize this display during the registration procedure after coarse registration. Points that are outside of the *Arm*'s workspace are highlighted in teal, and those that are at an angle too great to interface with the registration probe are black. For regions of the surface in which the registration probe can be activated with an incident angle of 10° or less, the surface of the model is colored green with greater intensity as the angle approaches 0° , indicating good-to-excellent interfacing between the surface and the registration probe. The operator is instructed to take care to sample broadly across the entire region of reachable locations to improve the

accuracy of the registration.

The heatmap is calculated after coarse alignment. First, we compute the the surface normal vectors at all vertices of the skin surface segmentation mesh. Next, we identify the approximate *Arm* mounting point A on the skull near Kocher's point, and we produce a second point B shifted one unit along the surface normal to approximate the rotational axis through the skull bolt. Next, we determine the optimal angle of incidence between the probe and each surface point. Because the links of the *Arm* distal to the bolt create a co-planar three-bar linkage, the probe workspace can be imagined as a subset of a plane that can rotate the identified axis. For each point X in the mesh, we calculate a plane that passes through A , B , and X , and the absolute angle between the normal N at X and the plane is calculated. We also identify whether X lies within the system's workspace via straightforward inverse kinematics calculated in the plane. The reachability and depression angle are color-coded as shown in Figure 5.

IV. EXPERIMENTAL DESIGN AND RESULTS

Our experiments evaluate four aspects of the system: bolt fixation rigidity, kinematic accuracy, end-to-end (kinematic, registration, and placement) accuracy, and *App* workflow usability in phantom user studies and ex-vivo ovine experiments.

A. Skull Bolt Fixation

To evaluate the quality of the bolt's fixation to the skull, we created a loading apparatus (Figure 6) to apply a maximum of 36.0 kg force at approximately 0° , 45° , or 90° offset from the axis of the skull bolt. The load with this apparatus is applied approximately 2.0 cm from the surface of the skull,

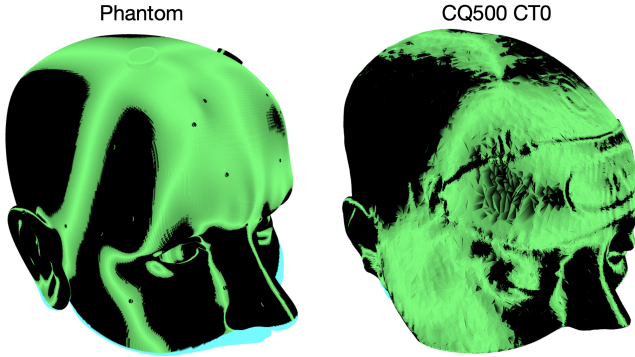


Fig. 5. Surface probe activation heatmap for the *Arm* when mounted at Kocher's Point. Activation angle is indicated by color, from low (bright green) to high (dim green), unreachable (black), and out of the *Arm*'s workspace (teal). Left side shows the testing phantom, and right side shows a patient CT scan from the CQ500 dataset [51]

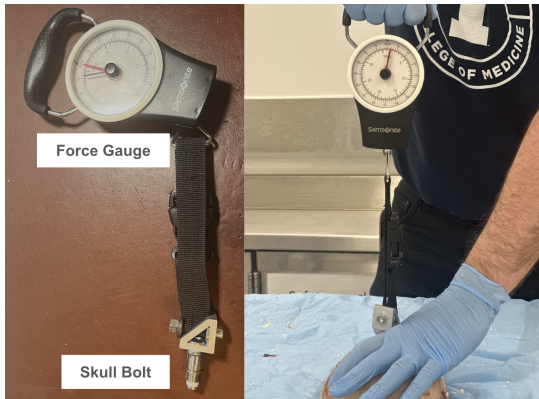


Fig. 6. Force gauge attached to the skull bolt for fixation study.

which results in approximately 7.06 Nm torque applied to the bolt under maximum load. We show evaluation on three skulls: an anatomical simulator skull cap (*Sawbones 1341-10*), a formaldehyde preserved human skull cap, and an alcohol preserved human skull cap. The bolt was placed at three calvarial points on the sawbones, and at the right Kocher's point in both of the human skull caps. Failure was defined as any bolt motion or loss of tension during loading. The results are shown in Table II.

Since the *Arm* weighs 348 g and the bolt embedded in cadaveric skull tissues support loads in excess of 36.0 kg without movement, we conclude that the *Arm* can be sufficiently supported by the rigid fixation the bolt provides in an adult skull.

TABLE II
BOLT LOADING ANALYSIS

| Load Angle | <i>Sawbones 1314-10</i> | Alcohol Preserved | Formaldehyde Preserved |
|------------|-------------------------|-------------------|------------------------|
| 0° | 35.5 | > 36.0 | > 36.0 |
| 45° | 23.3 | > 36.0 | > 36.0 |
| 90° | 17.6 | > 36.0 | > 36.0 |

* All measurements in kg

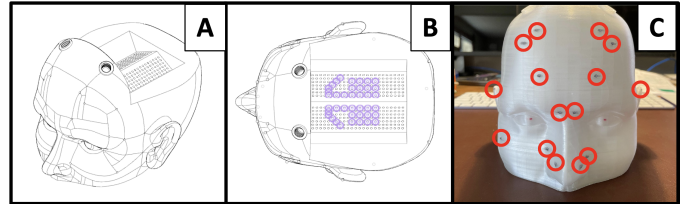


Fig. 7. 3D printed accuracy assessment phantom. A) 3D CAD Rendering of the phantom. B) Overhead view of Phantom. Target divots in purple are used for iTRE calculation. C) Target divots circled in red on the head phantom for sTRE calculation.

B. Kinematic Accuracy Evaluation

The accuracy of the *Arm* was evaluated using a 3D printed test fixture containing 20 measurement locations with which the effector of the device could directly interface. The purpose of this assessment is to evaluate “best case” repeatability and accuracy given the sensor accuracy and rigidity of the device. The rotary encoders have an angular accuracy of approximately 0.022°. The activation depth of the ball plunger switches used in our prototype is 1 mm, and allows for an additional 0.3 mm of travel beyond the activation depth to allow the probe to be activated at an angle from orthogonal to the incident surface. The repeatability of the *Arm* is found to be ± 0.042 mm (95% CI) in reaching the same position. The accuracy when comparing the difference between a measured position and the ground truth derived from the CAD model is measured to 1.688 ± 0.042 mm (95% CI). Experiments conducted to measure sensor accuracy can be found in the Supplementary Information.

C. End-to-End Accuracy Studies

In our second experiment, we designed and tested a 3D-printed medical phantom to evaluate the qualitative usability of the *App* and to perform quantitative assessment of the accuracy of our registration procedures.

Phantoms are employed to evaluate accuracy of the complete system and to provide a similar geometric context to the actual surgical procedure. Our phantoms enable a high-fidelity testing procedure so all components of the *App* and *Arm* can be unit-tested and refined. The phantom shown in Figure 7 contains realistic face geometry to perform surface registration, surface-mounted fiducial divots, and internal targets within the normal ventricular region of the head. Fiducial divots on the exterior surface serve as fiducials in the fiducial registration procedure and surface targets for evaluation of accuracy in all registration approaches. Surface targets are often utilized to confirm registration accuracy in craniofacial and neurosurgical procedures [52], and we explore their correspondence to targets closer to the surgical region of interest in these studies.

1) *Error Metrics - FRE and TRE*: Fiducial Registration Error (FRE) is calculated by determining the average error between corresponding points. The final mean absolute error (MAE) and root-mean squared error (RMSE) of distances between correspondences in PC2PC ICP and PC2SDF ICP is reported to represent the FRE.

Target Registration Error (TRE) is assessed for two feature sets: surface targets to assess registration accuracy, and targets near the area of interest to assess the error at the tip of a catheter mounted to the effector. Surface TRE (sTRE) is estimated by registering the navigation system to the phantom, then probing the points on the outside of the phantom and comparing the locations of these points to the location of the points as defined in the CAD File using MAE and RMSE.

We use a second ball plunger switch assembly, called the testing probe, to collect points at offset from the effector of the *Arm* for the purpose of estimating TRE at a point approximately where the tip of an EVD would be located relative to the effector of the system. The testing probe is offset by 120 mm from the effector of the system, and uses the same ball plunger switch as the registration probe, allowing it to interface with divots on the interior of the head phantom (Figure 7). Internal TRE (iTRE) is estimated by attaching the testing probe to the effector of the *Arm* and collecting the internal targets. Then the MAE and RMSE are computed between the divot positions as defined in the CAD model and the points collected with the testing probe.

2) *Registration accuracy:* In fiducial registration, six reachable random points in an ordered list are chosen as fiducials from the target point cloud as shown in Figure 7C, similar to skull-implanted fiducial registration [53]. The registration probe is placed in the divot at the target point and depressed, and the Cartesian position of the registration probe based on the forward kinematic calculation is saved to a list. This is repeated for each of the points, in the order prescribed by the randomly selected target points' list. Arun, et. al's approach to least-squares fitting is then applied to the moving (collected) and fixed (target) point clouds, and the resulting transform is applied to the base position of the AACMM [47]. We visually inspect alignment with the model in simulation, then all target and fiducial points are collected to estimate FRE and TRE.

In PC2PC ICP, the mesh of the patient skin surface is converted into a point cloud using a Poisson disk sampling method with 5000 points [49]. We perform coarse registration with the nose, nasion, and left brow, then trace the registration probe along the surface of the phantom, collecting points for every frame that the probe is activated until 2000 points are collected. We then register the traced points in the mesh-sampled point cloud using ICP with the PC2PC correspondence function described in Algorithms 1 and 2 (Figure 4). The MAE and RMSE between corresponding points in the point clouds from the final iteration are then calculated to estimate TRE.

In PC2SDF ICP, we use the same point collection procedures as in PC2PC ICP; however, we register the traced points in the mesh-sampled point cloud using ICP with the PC2SDF correspondence function described in Algorithms 1 and 3 (Figure 4). The MAE and RMSE between corresponding points in the point clouds from the final iteration are similarly calculated to estimate TRE.

We perform phantom testing for all three described registration methods, and FRE, sTRE, and iTRE are estimated for

TABLE III
FIDUCIAL AND SURFACE-BASED REGISTRATION METHOD ERRORS USING PHANTOMS (MAE)

| Method | FRE (mm) | sTRE (mm) | iTRE (mm) |
|------------|-------------------------------------|-------------------------------------|-------------------------------------|
| Fiducial | 0.838 ± 0.337 | 1.123 ± 0.316 | 1.744 ± 0.867 |
| PC2PC ICP | 5.990 ± 4.202 | 4.892 ± 4.076 | 3.246 ± 2.401 |
| PC2SDF ICP | 0.454 ± 0.275 | 3.182 ± 1.953 | 3.100 ± 1.637 |

* all intervals reported as 95% CI ($2 \times \text{SD}$) * bold: lowest error

TABLE IV
FIDUCIAL AND SURFACE-BASED REGISTRATION METHOD ERRORS USING PHANTOMS (RMSE)

| Method | FRE (mm) | sTRE (mm) | iTRE (mm) |
|------------|-------------------------------------|-------------------------------------|-------------------------------------|
| Fiducial | 0.895 ± 0.355 | 1.271 ± 0.471 | 1.811 ± 0.883 |
| PC2PC ICP | 6.960 ± 5.598 | 5.109 ± 4.314 | 3.357 ± 2.453 |
| PC2SDF ICP | 0.593 ± 0.358 | 3.310 ± 1.989 | 3.233 ± 1.736 |

* all intervals reported as 95% CI ($2 \times \text{SD}$) * bold: lowest error

each method. We performed 50% of trials for each method at Kocher's point on the left, and the other 50% on the right with randomized switching between sides on successive trials. We calculate MAE and RMSE for FRE, sTRE, and iTRE, reported in Tables III and IV. Collecting the point cloud is the rate-limiting step for performing registration, and the computational time for each registration method takes less than one second on our laptop. The tracing methodology between PC2PC and PC2SDF is identical. The time it takes an experienced operator to perform the tracing procedure with the laptop interface is 17.290 ± 6.233 s (95% CI). This is not statistically different from the time to complete the fiducial registration, which is 22.241 ± 22.346 s (95% CI).

D. Correlations Between Measured Errors

Using Pearson's correlation, FRE sTRE, and iTRE have slight to moderate correlations to each other in the PC2SDF registration method. We find that sTRE and iTRE are moderately correlated in the PC2PC registration method. The fiducial registration method showed little to no correlation between the measured errors (between -0.4 and 0.4). The Pearson correlations between all error measurements are reported in Table V.

TABLE V
PEARSON CORRELATION COEFFICIENTS BETWEEN ERRORS

| Method | FRE x sTRE | sTRE x iTRE | FRE x iTRE |
|----------|--------------|--------------|------------|
| Fid. M | 0.566 | 0.679 | 0.260 |
| PC2PC M | -0.081 | 0.549 | -0.259 |
| PC2SDF M | -0.078 | -0.121 | -0.197 |
| Fid. R | 0.511 | 0.743 | 0.253 |
| PC2PC R | -0.163 | 0.576 | -0.340 |
| PC2SDF R | -0.056 | -0.119 | -0.235 |

* Fid.=Fiducial; M=MAE; R=RMSE

* bold: moderate correlation; not bold: little to no correlation

We find significant differences in the accuracy of each method across all error metrics, except for the internal targets in both the PC2PC and PC2SDF methods, when using Student's t-tests comparing all methods. The iTRE in trials conducted at the left Kocher's Point versus right Kocher's Point additionally have statistically significant differences on a Student's t-test ($p < 0.01$). This difference in left vs. right is observed in the PC2SDF method for sTRE. We observed no other statistical differences in FRE, sTRE, or iTRE in these experiments.

1) Ex vivo Ovine Evaluation: To evaluate the accuracy of the proposed system in the context of real imaging and tissue, we performed the entire procedure on three ex vivo ovine heads (Figure 8). The heads were CT scanned preoperatively, and PC2SDF registration was used to evaluate the accuracy of 2 mm needles inserted into the brain under navigated visualization. The surface of the head is obtained with a Hounsfield unit threshold greater than -900. The nose tip, nasion, and left brow points are manually selected using 3D Slicer's markups module [45]. A 3D printed offset is used to position the tip of the needle at a 120mm offset from the effector of the navigation system. Once the needle is placed, the position of the tip of the needle is recorded relative to the registered navigation system. A postoperative CT image is then obtained and registered to the preoperative image using BRAINS 6 DOF registration in 3D Slicer [54], and we compare the measured and actual positions of the tip of the needle. We show six needle placements, two per head. The deviation between measured and actual needle tip positions is 2.765 ± 1.121 mm. We implanted the needles to an average depth of 42.23 ± 3.03 mm from the center of the outer skull aspect of the burr hole to the needle tip.

E. Pilot User Study

Three users are selected for our initial institutional review board approved pilot (UIUC IRB23-0316): a senior medical student applying to the neurosurgery match (User 1), a first-year medical student with minimal exposure to neurosurgery (User 2), and a neurosurgeon (User 3). This study evaluates the surface-based workflow with the PC2PC method only on the 3D printed phantom. We obtain consent from each user, and present them with a demonstration of workflow, followed by a 30 minute working session for the user to practice image registration and to ask questions about visual guidance with the tablet *App* and *Arm*. Following the working session, the users perform the bolting and registration workflows uninterrupted on the phantom for three trials each.

We collect the following criteria for each trial: bolt insertion time, coarse registration time per attempt, tracing registration time per attempt, time to align the virtual model of the EVD with the ventricles in simulation, total procedure time, and number of attempts until a successful registration (5 mm FRE or less). Means and standard deviations are shown in Table VI, indicating that all users attained sufficient proficiency to complete registration in 1 min and the full procedure within 2 min.

TABLE VI
WORKFLOW AND APP USABILITY TEST RESULTS

| Criteria | User 1 | User 2 | User 3 |
|--------------------------|-----------------|-----------------|-----------------|
| Bolt insertion (s) | 15.0 ± 3.8 | 17.0 ± 11.1 | 11.3 ± 4.2 |
| Coarse registration (s) | 3.0 ± 0.2 | 4.2 ± 1.8 | 5.8 ± 1.6 |
| Tracing registration (s) | 10.4 ± 0.5 | 9.6 ± 0.2 | 11.6 ± 1.9 |
| Registration attempts | 1.7 ± 1.2 | 1.0 ± 0.0 | 1.7 ± 0.6 |
| Drain alignment (s) | 5.2 ± 0.9 | 2.8 ± 0.7 | 7.9 ± 0.9 |
| Total time (s) | 56.8 ± 33.4 | 33.7 ± 11.5 | 70.1 ± 23.2 |

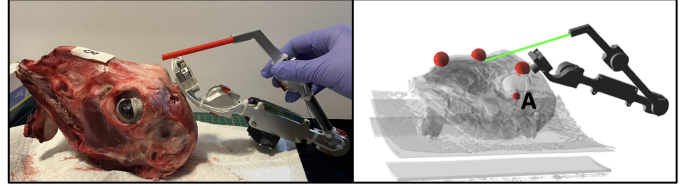


Fig. 8. Ovine carcass study and corresponding user interface visualization after registration and needle placement at point A. Nose tip, nasion, and left brow ridge shown as red spheres.

V. DISCUSSION

Overall, the design objectives outlined in Section I are met with our proposed system. Here, we analyze the experimental results in further detail to explore areas to potentially improve the system in the future.

Device accuracy. The results of our phantom study meets the expected procedural requirements for EVD placement using all three proposed registration methods based on the five design constraints: cost, time, accuracy, usability, and interactivity, and the ovine head study shows that this accuracy is maintained in real tissue. Fiducial registration significantly exceeds the accuracy of both PC2SDF and PC2PC registration (Tables III and IV). While the fiducial registration method clearly provides superior accuracy when compared to surface-based methods, in emergency conditions, an informed decision between the surgical workflows for fiducial and surface registration will be required as fiducial registration has a more involved surgical setup. The repetition of high accuracy results in our ovine head evaluation further affirms these findings.

Relation between accuracy and mounting location. We note differences in accuracy between the left Kocher's Point and the right, with the left Kocher's Point having statistically significantly higher error than the right. This may be attributed to differences in expertise in performing the procedure on the left and right, and differences in the testing probe interfacing between targets chosen for the left and right point clouds. The operator for the phantom experiments is skilled at performing the procedure with their dominant (right) hand with the *Arm* mounted on the right Kocher's Point, and is less experienced at performing the procedure with their non-dominant (left) hand with the *Arm* mounted on the left Kocher's Point. Therefore, the operator may have inadvertently increased error at the left Kocher's point through increased force on the bearings, which increases axial deviation, thereby increasing the error at the

effector. The testing probe did not interface as well with the selected internal targets on the left side as opposed to the right. This may have been due to differences in the threads created by the self-tapping bolt on the left and right Kocher's points. It is noted that the bolt axis may not perfectly align with the burr hole axis, which is mitigated by registration, but results in difficulty reaching pre-planned target points, particularly in the internal target region.

Registration correlations. The lack of a significant difference between PC2PC and PC2SDF iTRE suggests that the procedural accuracy between both PC2PC and PC2SDF are comparable, despite the observed statistical differences in sTRE between the methods. This may also indicate that sTRE, while used clinically in other neuronavigation systems, may not be a sufficient error metric to confirm accuracy of a given registration. This additionally suggests that either PC2PC or PC2SDF would be sufficient for surgical navigation, as both methods are accurate enough for the clinical scenario of EVD placement within a 5 mm tolerance, and both are sufficiently computationally optimized for a low-power laptop to quickly process the data. Some methods seemed to show a correlation between FRE and sTRE. Both sTRE and iTRE measurements were moderately correlated for the Fiducial and PC2PC registration methods, however they were uncorrelated for the PC2SDF method. Previous work by Fitzpatrick, et al. indicates that correlations between FRE and TRE are not expected [55]. Therefore, we anticipate that more experiments on our kinematic navigation system would provide a greater distribution in these errors, reducing correlations.

Ovine versus human accuracy. The results show RMSE of 2.765 ± 1.121 mm in ovine heads, and 3.357 ± 2.453 mm in human phantom models with the same registration approach (Table IV and Figure 8). This result is expected, because an ovine head has more geometrically distinctive features compared to a human head, reducing the ambiguity in rotation with iterative registration methods. The targets in the ovine models are also relatively closer to the registration surface compared to the deeper targets in the human phantom. Hence, it follows that accuracy would be moderately improved in ovine models over human models, as seen in these experiments.

Limitations. A notable limitation is that our accuracy evaluations did not evaluate the effects of deformation expected from skin under the registration probe, since the phantom was made from rigid PLA plastic and the ovine heads were skinned. Further work will have to be conducted to assess the extent of deformation caused by the registration probe and its affect on registration accuracy. The activation force for the current registration probe is 1 N which would likely cause non-negligible skin deformation. Future designs could investigate contact sensors with lower activation forces.

During repeated use, the bearings used in the *Arm* began to exhibit small axial deviations which resulted in lower effector accuracy. The probe used to collect internal target points is able to bend by approximately 2 millimeters from its expected position when interfaced with a given point, which may result in increased error when collecting points at each of the internal

targets on the phantom. A similar bending issue is expected in an EVD, because the stylet does not make the drain perfectly rigid. Future work will be required to quantify these bending errors.

The *Arm* in its current form cannot be sterilized due to use of 3D printed parts, and will require further work to determine an appropriate solution to sterilization, including the potential for the *Arm* to be sterilized in an autoclave, use of alcohol for disinfection, or use of disposable sterile sleeves and components. The registration probe and bolt will additionally have to interface with patient tissue, and may pose infection risks. Further design and live animal evaluations will be required to quantify and mitigate risks of infection.

VI. CONCLUSIONS AND FUTURE WORK

We present a low-cost real-time neurosurgical navigation system designed to be rigidly bolted to a patient's skull and operated rapidly in emergent settings. The system is capable of achieving sufficient accuracy using both fiducial and surface-based registration workflows, can be added to bedside surgical workflows consistently in under 2 minutes. Even novice medical trainees are capable of learning to use this system in under 30 minutes of training. Our evaluation provides evidence that our device can meet the accuracy needs for the EVD placement procedure and other stereotactic neurosurgery procedures. The total cost of production and material for the prototype is less than \$2,500, suggesting potential use in underserved settings.

We plan to continue our human subjects user study, in which various providers including nurses, medical students, and various physician specialists will perform EVD placement procedures in phantoms and cadavers and the accuracy of EVD placements will be compared between training levels. Automated segmentation, target selection, and graphical user interface refinements will be incorporated into these user interface trials. Future work will also address the limitations discussed, particularly sterilization of the device and reduction of the activation force of the registration probe to minimize the impact of skin deformation on registration accuracy. Further animal and cadaver studies will be conducted with approval from our university's institutional animal care and use committee to validate safety and infection risks associated with the use of this system.

VII. ACKNOWLEDGMENT

We would like to thank Sarah Van Note and Dallas Fredrick for their support in obtaining 3D imaging. We thank Dr. Wessam Ibrahim and Dr. J. P. Swigart for assisting in the design and conduct of bolt force testing on cadavers at the Carle Illinois College of Medicine anatomy laboratory. We thank Aarthi Balaji, Billy Burek, Nathan Jacobs, and Ellen Yang for their assistance developing the tablet user interface. We also thank Charee Thompson for her assistance in user study design. Research reported in this publication is supported by the National Institute of Biomedical Imaging and Bioengineering of the National Institutes of Health under award number NIH 1F30EB035932-01.

REFERENCES

- [1] A. Cohen-Gadol. "External ventricular drain," Neurosurgical Atlas. (), [Online]. Available: <https://www.neurosurgicalatlas.com/volumes/csf-diversion-procedures/external-ventricular-drain> (visited on 12/12/2023).
- [2] R. Muralidharan. "External ventricular drains: Management and complications," eng, *Surgical Neurology International*, vol. 6, no. Suppl 6, S271–274, 2015.
- [3] S. Hagel, T. Bruns, M. W. Pletz, C. Engel, R. Kalff, and C. Ewald, "External Ventricular Drain Infections: Risk Factors and Outcome," *Interdisciplinary Perspectives on Infectious Diseases*, vol. 2014, A. Eid, Ed., p. 708531, Nov. 2014, Publisher: Hindawi Publishing Corporation. [Online]. Available: <https://doi.org/10.1155/2014/708531>.
- [4] C. Miller and R. P. Tummala, "Risk factors for hemorrhage associated with external ventricular drain placement and removal," *Journal of Neurosurgery JNS*, vol. 126, no. 1, pp. 289–297, 2017. [Online]. Available: <https://thejns.org/view/journals/j-neurosurg/126/1/article-p289.xml>.
- [5] J. B. G. Ghajar, "A guide for ventricular catheter placement," Dec. 1, 1985, Section: *Journal of Neurosurgery*. [Online]. Available: <https://thejns.org/view/journals/j-neurosurg/63/6/article-p985.xml> (visited on 06/10/2024).
- [6] A. Enriquez-Marulanda, L. C. Ascanio, M. M. Salem, G. A. Maragos, R. Jhun, A. Y. Alturki, J. M. Moore, C. S. Ogilvy, and A. J. Thomas, "Accuracy and safety of external ventricular drain placement by physician assistants and nurse practitioners in aneurysmal acute subarachnoid hemorrhage," *Neurocritical Care*, vol. 29, no. 3, pp. 435–442, Dec. 2018.
- [7] A. AlAzri, K. Mok, J. Chankowsky, M. Mullah, and J. Marcoux, "Placement accuracy of external ventricular drain when comparing freehand insertion to neuronavigation guidance in severe traumatic brain injury," eng, *Acta Neurochirurgica*, vol. 159, no. 8, pp. 1399–1411, Aug. 2017.
- [8] A. K. Toma, S. Camp, L. D. Watkins, J. Grieve, and N. D. Kitchen, "External ventricular drain insertion accuracy: Is there a need for change in practice?" *Neurosurgery*, vol. 65, no. 6, 1197–1200; discussion 1200–1201, Dec. 2009.
- [9] S. B. Phillips, M. Gates, and S. Krishnamurthy, "Strategic placement of bedside ventriculostomies using ultrasound image guidance: Report of three cases," eng, *Neurocritical Care*, vol. 17, no. 2, pp. 255–259, Oct. 2012.
- [10] J. H. Manfield and K. K. H. Yu, "Real-time ultrasound-guided external ventricular drain placement: Technical note," en, Nov. 2017, Section: *Neurosurgical Focus*. [Online]. Available: <https://thejns.org/focus/view/journals/neurosurg-focus/43/5/article-pE5.xml> (visited on 01/16/2025).
- [11] H. Bow, L. He, M. A. Raees, S. Pruthi, and R. Chitale, "Development and implementation of an inexpensive, easily producible, time efficient external ventricular drain simulator using 3-dimensional printing and image registration," *Operative Neurosurgery (Hagerstown, Md.)*, vol. 16, no. 4, pp. 496–502, Apr. 1, 2019.
- [12] S.-Y. Yoon, Y. Kwak, and J. Park, "Adjustable Ghajar Guide Technique for Accurate Placement of Ventricular Catheters: A Pilot Study," *Journal of Korean Neurosurgical Society*, vol. 60, no. 5, pp. 604–609, Sep. 2017. [Online]. Available: <https://www.ncbi.nlm.nih.gov/pmc/articles/PMC5594620/> (visited on 01/16/2025).
- [13] G. E. Umana, G. Scalia, K. Yagmurlu, R. Mineo, S. Di Bella, M. Giunta, A. Spitaleri, R. Maugeri, F. Graziano, M. Fricia, G. F. Nicoletti, S. O. Tomasi, G. Raudino, B. Chaurasia, G. Bellocchi, M. Salvati, D. G. Iacopino, S. Cicero, M. Visocchi, and L. Strigari, "Multimodal simulation of a novel device for a safe and effective external ventricular drain placement," *Frontiers in Neuroscience*, vol. 15, 2021. [Online]. Available: <https://www.frontiersin.org/journals/neuroscience/articles/10.3389/fnins.2021.690705> (visited on 02/13/2024).
- [14] A. S. Barath, A. E. Rusheen, J. M. R. Cabrera, H. Shin, C. D. Blaha, K. E. Bennet, S. J. Goerss, K. H. Lee, and Y. Oh, "Development and validation of a rapidly deployable CT-guided stereotactic system for external ventricular drainage: Preclinical study," en, *Scientific Reports*, vol. 11, no. 1, p. 17492, Sep. 2021, Publisher: Nature Publishing Group. [Online]. Available: <https://www.nature.com/articles/s41598-021-97080-2> (visited on 01/16/2025).
- [15] M. Spadola, N. Muhammad, S. Ajmera, R. Jabarkheel, S. Tomlinson, S. P. Miranda, M. S. Grady, J. Schuster, and R. Blue, "The Device for Intraventricular Entry guide: A novel solution to a perpetual problem," eng, *Journal of Neurosurgery*, vol. 140, no. 5, pp. 1501–1506, May 2024.
- [16] A. Daniel, M. Coronel, S. Peer, B. Grinshpan, S. Duru, J. L. Peiro, J. L. Leach, E. Abelln, C. M. Doerning, D. Zarrouk, and F. T. Mangano, "A novel minimally invasive neurosurgical cranial fixation device for improved accuracy of intraventricular catheter placement: An experimental animal study," *Patient Safety in Surgery*, vol. 18, no. 1, p. 36, Dec. 2024. [Online]. Available: <https://doi.org/10.1186/s13037-024-00420-0> (visited on 01/16/2025).
- [17] S. Liang, R. Z. Lee, Y. G. Lim, H. Lim, F. Misbaah, and K. R. Wan, "Improving Successful Cannulation of External Ventricular Drain: 3D-Printed Surgical Guide for Inexperienced Neurosurgeons," *World Neurosurgery*, vol. 193, pp. 715–721, Jan. 2025. [Online]. Available: <https://www.sciencedirect.com/science/article/pii/S1878875024016851> (visited on 01/16/2025).
- [18] M. J. Stuart, J. Antony, T. K. Withers, and W. Ng, "Systematic review and meta-analysis of external ventricular drain placement accuracy and narrative review of guidance devices," English, *Journal of Clinical Neuroscience*, vol. 94, pp. 140–151, Dec. 2021, Publisher: Elsevier. [Online]. Available: [https://www.jocn-journal.com/article/S0967-5868\(21\)00521-X/fulltext](https://www.jocn-journal.com/article/S0967-5868(21)00521-X/fulltext) (visited on 12/12/2023).
- [19] A. I. R. Maas *et al.*, "Traumatic brain injury: Integrated approaches to improve prevention, clinical care, and research," *The Lancet Neurology*, vol. 16, no. 12, pp. 987–1048, Dec. 1, 2017, Publisher: Elsevier. [Online]. Available: [https://www.thelancet.com/journals/laneur/article/PIIS1474-4422\(17\)30371-X/abstract](https://www.thelancet.com/journals/laneur/article/PIIS1474-4422(17)30371-X/abstract) (visited on 03/11/2024).
- [20] A. Khoshnevisan and N. S. Allahabadi, "Neuronavigation: Principles, clinical applications and potential pitfalls," *Iranian Journal of Psychiatry*, vol. 7, no. 2, pp. 97–103, 2012. [Online]. Available: <https://www.ncbi.nlm.nih.gov/pmc/articles/PMC3428645/> (visited on 02/13/2024).
- [21] R. Schreurs, F. Baan, C. Klop, L. Dubois, L. F. M. Beenken, P. E. M. H. Habets, A. G. Becking, and T. J. J. Maal, "Registration-free workflow for electromagnetic and optical navigation in orbital and craniofacial surgery," *Scientific Reports*, vol. 11, no. 1, p. 18080, Sep. 10, 2021, Publisher: Nature Publishing Group. [Online]. Available: <https://www.nature.com/articles/s41598-021-97706-5> (visited on 03/07/2024).
- [22] X. Chen, L. Xu, Y. Wang, H. Wang, F. Wang, X. Zeng, Q. Wang, and J. Egger, "Development of a surgical navigation system based on augmented reality using an optical see-through head-mounted display," *Journal of Biomedical Informatics*, vol. 55, pp. 124–131, Jun. 2015.
- [23] M. Huang, T. A. Tetreault, A. Vaishnav, P. J. York, and B. N. Staub, "The current state of navigation in robotic spine surgery," *Annals of Translational Medicine*, vol. 9, no. 1, pp. 86–86, Jan. 2021, Number: 1 Publisher: AME Publishing Company. [Online]. Available: <https://atm.amegroups.org/article/view/46418> (visited on 03/07/2024).
- [24] A. M. Kadi, L. J. Zamorano, M. P. Frazer, and Y. Lu, "Design and simulation of an articulated surgical arm for guiding stereotactic neurosurgery," vol. 1708, pp. 400–417, Mar. 1, 1992, Conference Name: Applications of Artificial Intelligence X: Machine Vision and Robotics ADS Bibcode: 1992SPIE.1708..400K. [Online]. Available: <https://ui.adsabs.harvard.edu/abs/1992SPIE.1708..400K> (visited on 03/07/2024).
- [25] N. Hayashi, S. Endo, H. Ikeda, and A. Takaku, "Neuronavigation using an articulated arm with a bayonet probe on a computer graphic composite of magnetic resonance and computerized tomography images," *Minimally invasive neurosurgery: MIN*, vol. 41, no. 3, pp. 144–148, Sep. 1998.
- [26] R. Rohling, P. Munger, J. M. Hollerbach, and T. Peters, "Comparison of relative accuracy between a mechanical and an optical position tracker for image-guided neurosurgery," *Computer Aided Surgery*, vol. 1, no. 1, pp. 30–34, Jan. 1995. [Online]. Available: <http://www.tandfonline.com/doi/full/10.3109/10929089509106823> (visited on 03/07/2024).
- [27] S. Gutmann, C. Tstensen, I. C. Bttcher, J. Dietzel, S. Loderstedt, S. Kohl, K. Matiasek, and T. Flegel, "Clinical use of a new frameless optical neuronavigation system for brain biopsies: 10 cases (20132020)," *Journal of Small Animal Practice*, vol. 63, no. 6, pp. 468–481, 2022, eprint: <https://onlinelibrary.wiley.com/doi/pdf/10.1111/jsap.13482>. [Online]. Available: <https://onlinelibrary.wiley.com/doi/abs/10.1111/jsap.13482> (visited on 03/07/2024).
- [28] V. Patil, R. Gupta, R. S. J. Estpar, R. Lacson, A. Cheung, J. M. Wong, A. J. Popp, A. Golby, C. Ogilvy, and K. G. Vosburgh, "Smart stylet:

- The development and use of a bedside external ventricular drain image-guidance system," *Stereotactic and functional neurosurgery*, vol. 93, no. 1, pp. 50–58, 2015. [Online]. Available: <https://www.ncbi.nlm.nih.gov/pmc/articles/PMC4423620/> (visited on 03/07/2024).
- [29] P. S. Upadhyayula, J. K. Yue, J. Yang, H. S. Birk, and J. D. Ciacchi, "The current state of rural neurosurgical practice: An international perspective," *Journal of Neurosciences in Rural Practice*, vol. 9, no. 1, pp. 123–131, 2018. [Online]. Available: <https://www.ncbi.nlm.nih.gov/pmc/articles/PMC5812136/>.
- [30] . Lger, S. Horvath, J.-C. Fillion-Robin, D. Allemand, S. Gerber, P. Juvekar, E. Torio, T. Kapur, S. Pieper, S. Pujol, R. Bardsley, S. Frisken, and A. Golby, "NousNav: A low-cost neuronavigation system for deployment in lower-resource settings," *International Journal of Computer Assisted Radiology and Surgery*, vol. 17, no. 9, pp. 1745–1750, Sep. 2022.
- [31] J. Park, W. Son, K.-S. Park, M. Y. Kim, and J. Lee, "Calvarial slope affecting accuracy of ghajar guide technique for ventricular catheter placement," *Journal of Neurosurgery*, vol. 124, no. 5, pp. 1429–1433, May 2016.
- [32] A. D. Smith, A. J. Teague, A. Naik, M. Janbahan, E. J. Smith, D. T. Krist, S. Parupalli, K. Teal, and W. Hassaneen, "Robotic external ventricular drain placement for acute neurosurgical care in low-resource settings: Feasibility considerations and a prototype design," EN, *Neurosurgical Focus*, vol. 52, no. 1, E14, Jan. 2022, Publisher: American Association of Neurological Surgeons Section: Neurosurgical Focus. [Online]. Available: <https://thejns.org/focus/view/journals/neurosurg-focus/52/1/article-pE14.xml> (visited on 12/12/2023).
- [33] S. Rajasekaran, D. C. Raja, and A. P. Shetty, "Section 11, chapter 14: Navigation in spine surgery," Wheeless' Textbook of Orthopaedics. (Jan. 1, 2018), [Online]. Available: <https://www.wheelineonline.com/issls/section-11-chapter-14-navigation-in-spine-surgery/> (visited on 03/07/2024).
- [34] W. K. Pfisterer, S. Papadopoulos, D. A. Drumm, K. Smith, and M. C. Preul, "Fiducial versus nonfiducial neuronavigation registration assessment and considerations of accuracy," *Neurosurgery*, vol. 62, no. 3, 201–207; discussion 207–208, Mar. 2008.
- [35] J. Fitzpatrick, J. West, and C. Maurer, "Predicting error in rigid-body point-based registration," *IEEE Transactions on Medical Imaging*, vol. 17, no. 5, pp. 694–702, Oct. 1998, Conference Name: IEEE Transactions on Medical Imaging. [Online]. Available: <https://ieeexplore.ieee.org/document/736021> (visited on 02/13/2024).
- [36] R. Krishnan, E. Hermann, R. Wolff, M. Zimmermann, V. Seifert, and A. Raabe, "Automated fiducial marker detection for patient registration in image-guided neurosurgery," *Computer Aided Surgery: Official Journal of the International Society for Computer Aided Surgery*, vol. 8, no. 1, pp. 17–23, 2003.
- [37] K. Chen, L. M. Lui, and J. Modersitzki, "Chapter 15 - image and surface registration," in *Processing, Analyzing and Learning of Images, Shapes, and Forms: Part 2*, ser. Handbook of Numerical Analysis, R. Kimmel and X.-C. Tai, Eds., vol. 20, ISSN: 1570-8659, Elsevier, 2019, pp. 579–611. [Online]. Available: <https://www.sciencedirect.com/science/article/pii/S1570865919300146>.
- [38] R. Zamora, S. E. Punt, C. Christman-Skieller, C. Yildirim, J. C. Shapton, and E. U. Conrad, "Are skin fiducials comparable to bone fiducials for registration when planning navigation-assisted musculoskeletal tumor resections in a cadaveric simulated tumor model?" *Clinical Orthopaedics and Related Research*, vol. 477, no. 12, pp. 2692–2701, Dec. 2019. [Online]. Available: <https://www.ncbi.nlm.nih.gov/pmc/articles/PMC6907307/>.
- [39] Saint Louis University, *2019 Senior Design Projects*. St. Louis, MO, USA: Saint Louis University, 2019, pp. 54–55.
- [40] M. Borovik, "Cost effective neurosurgical navigation with a passive robot for external ventricular drain placement," English, Copyright - Database copyright ProQuest LLC; ProQuest does not claim copyright in the individual underlying works; Last updated - 2023-09-15, Ph.D. dissertation, 2021, p. 125. [Online]. Available: <https://www-proquest-com.proxy2.library.illinois.edu/dissertations-theses/cost-effective-neurosurgical-navigation-with/docview/2593058390/se-2>.
- [41] P. J. Morone, M. C. Dewan, S. L. Zuckerman, R. S. Tubbs, and R. J. Singer, "Craniometrics and ventricular access: A review of kocher's, kaufman's, paine's, menovksy's, tubbs, keen's, frazier's, dandy's, and sanchez's points," *Operative Neurosurgery*, vol. 18, no. 5, p. 461, May 2020. [Online]. Available: https://journals-lww-com.proxy2.library.illinois.edu/onsonline/fulltext/2020/05000/com.proxy2.library.illinois.edu/onsonline/fulltext/2020/05000/craniometrics_and_ventricular_access_a_review_of_1.aspx (visited on 07/03/2024).
- [42] R. Balachandran, M. A. Fritz, M. S. Dietrich, A. Danilchenko, J. E. Mitchell, V. L. Oldfield, W. W. Lipscomb, J. M. Fitzpatrick, J. S. Neimat, P. E. Konrad, and R. F. Labadie, "Clinical testing of an alternate method of inserting bone-implanted fiducial markers," *International journal of computer assisted radiology and surgery*, vol. 9, no. 5, pp. 913–920, Sep. 2014. [Online]. Available: <https://www.ncbi.nlm.nih.gov/pmc/articles/PMC4431776/> (visited on 07/05/2024).
- [43] L. Lenchik, L. Heacock, A. A. Weaver, R. D. Boutin, T. S. Cook, J. Itri, C. G. Filippi, R. P. Gullapalli, J. Lee, M. Zagurovskaya, T. Retson, K. Godwin, J. Nicholson, and P. A. Narayana, "Automated segmentation of tissues using CT and MRI: A systematic review," *Academic radiology*, vol. 26, no. 12, pp. 1695–1706, Dec. 2019. [Online]. Available: <https://www.ncbi.nlm.nih.gov/pmc/articles/PMC6878163/> (visited on 03/07/2024).
- [44] A. Irimia, A. S. Maher, K. A. Rostovsky, N. F. Chowdhury, D. H. Hwang, and E. M. Law, "Brain segmentation from computed tomography of healthy aging and geriatric concussion at variable spatial resolutions," *Frontiers in Neuroinformatics*, vol. 13, Mar. 18, 2019, Publisher: Frontiers. [Online]. Available: <https://www.frontiersin.org/articles/10.3389/fninf.2019.00009> (visited on 03/07/2024).
- [45] A. Fedorov, R. Beichel, J. Kalpathy-Cramer, J. Finet, J.-C. Fillion-Robin, S. Pujol, C. Bauer, D. Jennings, F. Fennessy, M. Sonka, J. Buatti, S. Aylward, J. V. Miller, S. Pieper, and R. Kikinis, "3d slicer as an image computing platform for the quantitative imaging network," *Magnetic resonance imaging*, vol. 30, no. 9, pp. 1323–1341, Nov. 2012. [Online]. Available: <https://www.ncbi.nlm.nih.gov/pmc/articles/PMC3466397/> (visited on 06/11/2024).
- [46] W. Schroeder, R. Maynard, and B. Geveci, "Flying edges: A high-performance scalable isocontouring algorithm," in *2015 IEEE 5th Symposium on Large Data Analysis and Visualization (LDAV)*, 2015, pp. 33–40.
- [47] K. S. Arun, T. S. Huang, and S. D. Blostein, "Least-squares fitting of two 3-d point sets," *IEEE transactions on pattern analysis and machine intelligence*, vol. 9, no. 5, pp. 698–700, May 1987.
- [48] P. Besl and N. D. McKay, "A method for registration of 3-d shapes," *IEEE Transactions on Pattern Analysis and Machine Intelligence*, vol. 14, no. 2, pp. 239–256, Feb. 1992, Conference Name: IEEE Transactions on Pattern Analysis and Machine Intelligence. [Online]. Available: <https://ieeexplore.ieee.org/document/121791>.
- [49] Q.-Y. Zhou, J. Park, and V. Koltun, *Open3d: A modern library for 3d data processing*, Jan. 29, 2018. [Online]. Available: <http://arxiv.org/abs/1801.09847> (visited on 03/07/2024).
- [50] C. Yuksel, "Sample elimination for generating poisson disk sample sets," 2015, Publisher: The Eurographics Association and John Wiley & Sons Ltd. [Online]. Available: <https://doi.org/10.1111/cgf.12538> (visited on 07/05/2024).
- [51] S. Chilamkurthy, R. Ghosh, S. Tanamala, M. Biviji, N. G. Campeau, V. K. Venugopal, V. Mahajan, P. Rao, and P. Warier, "Deep learning algorithms for detection of critical findings in head CT scans: A retrospective study," *Lancet (London, England)*, vol. 392, no. 10162, pp. 2388–2396, Dec. 1, 2018.
- [52] M. N. Wang and Z. J. Song, "Properties of the target registration error for surface matching in neuronavigation," *Computer Aided Surgery: Official Journal of the International Society for Computer Aided Surgery*, vol. 16, no. 4, pp. 161–169, 2011.
- [53] M. Ivanov and A. Vlad Ciurea, "Neuronavigation. principles. surgical technique.," *Journal of Medicine and Life*, vol. 2, no. 1, pp. 29–35, 2009. [Online]. Available: <https://www.ncbi.nlm.nih.gov/pmc/articles/PMC5051478/>.
- [54] H. Johnson, G. Harris, and K. Williams, "BRAINSFit: Mutual Information Registrations of Whole-Brain 3D Images, Using the Insight Toolkit," *The Insight Journal*, Oct. 2007. [Online]. Available: <https://www.insight-journal.org/browse/publication/180>.
- [55] J. M. Fitzpatrick, "Fiducial registration error and target registration error are uncorrelated," in *Medical Imaging 2009: Visualization, Image-Guided Procedures, and Modeling*, vol. 7261, SPIE, Mar. 13, 2009, pp. 21–32. [Online]. Available: <https://www.spiedigitallibrary.org/conference-proceedings-of-spie/7261/726102/Fiducial-registration-error-and-target-registration-error-are-uncorrelated/10.1117/12.813601.full> (visited on 03/07/2024).

VIII. SUPPLEMENTAL EXPERIMENTS

A. AACMM Accuracy Studies and Analysis

Our test fixture is designed to evaluate kinematic properties of the *Arm*, including encoder noise, repeatability, and accuracy when propagated through the kinematic model (Figure 9A).

B. Testing equipment tolerances

The optical breadboards (Thorlabs, Newton, NJ) used had a machining tolerance of 0.006 mm. A Mars 3 Pro 3D printer (Elegoo, Shenzhen, Guangdong, China) is used to make calibration standoffs that interface with the navigation system with a layer tolerance of 0.05 mm, accounting for a linear resin shrinkage of 1.25% as measured on this specific machine with the resin used. All interfaces with the navigation system are designed perpendicular to the printed layers of the 3D printed components to utilize the most accurate printed dimension of the part. The standoff breadboard and phantoms (Figure 7) used to assess system accuracy and TRE are printed using an Ender 5 S1 (Creality, Shenzhen, Guangdong, China) with a dimensional accuracy of 0.2 mm in X, Y, and Z. All relevant surfaces have been measured with a precision micrometer and sanded to the appropriate size as needed to ensure calibration and measurement accuracy.

C. Sensor Accuracy Assessments

The reported accuracy of the 14-bit encoders is 0.2° . However, if individual encoders are calibrated, the actual worst-case accuracy is expected to be approximately 0.022° , which is tested by measuring the angular repeatability of individual calibrated encoders. Repeatability analysis is conducted by connecting the encoder to an optical breadboard with a metal rod perpendicular to the axis of rotation, and each of the four encoders is rotated between two metal rods attached to the optical breadboard and offset by 90° to each other. The encoder is rotated between the two rods and the error in measuring the angle is reported across 50 trials for each of the four encoders used in the *Arm*. Encoder 1 interfaces between the first link and the skull bolt, and encoder 4 interfaces

between the two distal links. Each encoder gate should have an activated range of 0.022° on the encoders, and we find that each encoder measures within this range in our experimental setup.

The reported activation depth of the registration probe and testing probe is 1 mm, and allows for an additional 0.3 mm of depth beyond the activation depth to allow the probes to be activated at an angle from orthogonal to the incident surface. These activation depths are tested using a micrometer and through phantom experimentation.

1) *Calibration procedure:* The system is calibrated to a home position using standoffs as shown in Figure 9A. When the *Arm* is positioned the home position, 100 frames from the three most distal encoders are averaged to account for vibratory noise, and each angle is subtracted from its corresponding value in software to define the zero position of each encoder. Because registration would account for any rotation about the skull bolt, the encoder measuring the angular position of the skull bolt does not require calibration.

2) *Coordinate Measuring accuracy:* After calibration, the worst-case position error in simulation is expected to be 0.268 mm at the effector when propagated through the forward kinematic model, using the calibrated encoder accuracy of 0.022° .

Three kinematic properties of the *Arm* are measured: the noise of the effector relative to the base, the repeatability of the *Arm* in reaching the same positions over a number of measurements, and the accuracy in measuring a specified position relative to the base. These properties are evaluated using the optical breadboard-mounted test-fixture seen in Figure 9A by 1) mounting the *Arm* and calibrating the home position of all four encoders, 2) slotting the posts into the effector of the *Arm* 3) measuring noise for 500 frames at the post 9B, 4) computing the average position of the effector at that location, and 5) recording these positions across all 20 posts for a total of 40 trials (800 total measurements). Repeatability is reported as a 95% confidence interval (CI) for the differences between the ground truth and measured positions (Figure 9C), and accuracy is reported as the mean of these differences (Figure 9D).

The noise of the *Arm* effector position is measured to be ± 0.0066 mm (95% CI) from a given mean position 9B. The repeatability of the *Arm* is found to be ± 0.042 mm (95% CI) in reaching the same position on any given post. The accuracy measurement when comparing the difference between measured position and position in the CAD file is found to be 1.688 ± 0.042 mm (95% CI).

IX. SUPPLEMENTAL DISCUSSION

Device Accuracy. The accuracy of 1.688 mm in our breadboard evaluation could be due to several sources of systematic error. We find that the majority of the error is found in the horizontal (y) axis, likely due to a rotational error caused by the calibration procedure used in this setup, indicated by the small repeatability range of ± 0.042 mm. Another possible source of error in these tests is physical shifts in the calibration target positions due to the use of 3D printing.

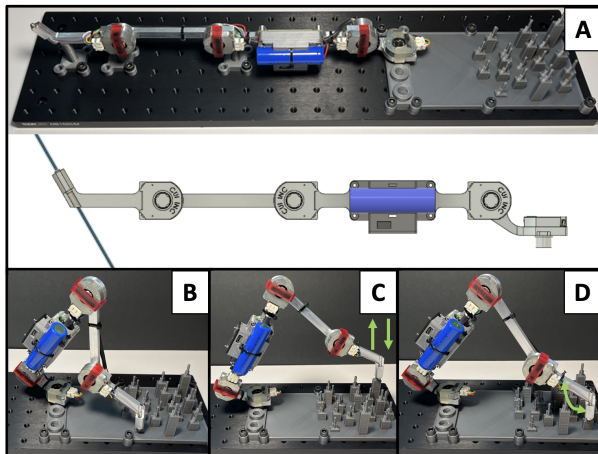


Fig. 9. Breadboard testing procedures. A) Home position calibration. B) Stable position noise measurement. C) Repeatability measurement. D) Accuracy measurement.